Multi-component chemo-mechanics based on transport relations for the chemical potential

P. Shanthraj[a,b,*], C. Liu[b,**], A. Akbarian[b,c], B. Svendsen[b,c], D. Raabe[b]

[a] *The Department of Materials, The University of Manchester, Manchester M1 3BB, UK*
[b] *Max-Planck-Institut für Eisenforschung, Max-Planck-Straße 1, 40237 Düsseldorf, Germany*
[c] *Material Mechanics, RWTH Aachen University, Schinkelstraße 2, 52062 Aachen, Germany*

Abstract

A chemo-mechanical model for a finite-strain elasto-viscoplastic material containing multiple chemical components is formulated and an efficient numerical implementation is developed to solve the resulting transport relations. The numerical solution relies on inverting the constitutive model for the chemical potential. In this work, a semi-analytical inversion for a general family of multi-component regular-solution chemical free energy models is derived. This is based on splitting the chemical free energy into a convex contribution, treated implicitly, and a non-convex contribution, treated explicitly. This results in a reformulation of the system transport equations in terms of the chemical potential rather than the composition as the independent field variable. The numerical conditioning of the reformulated system, discretised by finite elements, is shown to be significantly improved, and convergence to the Cahn–Hilliard solution is demonstrated for the case of binary spinodal decomposition. Chemo-mechanically coupled binary and ternary spinodal decomposition systems are then investigated to illustrate the effect of anisotropic elastic deformation and plastic relaxation of the resulting spinodal morphologies in more complex material systems.
ⓒ 2020 The Author(s). Published by Elsevier B.V. This is an open access article under the CC BY license (http://creativecommons.org/licenses/by/4.0/).

Keywords: Multi-component; Spinodal decomposition; Chemo-mechanics; Crystal plasticity

1. Introduction

The main goal of modern materials science is the theory-guided tailoring of materials, including chemical composition and microstructure, in order to obtain improved properties for a sustainable technological development. While there has been a tremendous growth over recent years in the use of modelling and simulation tools towards this goal [1–4], the realistic prediction of the thermo-chemo-mechanical interactions relevant to industrial processes is still a key development required to enable technological advances in material design, manufacturing and product development for harsh-service environments. It is recognised that the interaction of solute diffusion and elasto-plastic deformation plays a prominent role in the microstructural evolution and the subsequent performance in a

---

wide range of materials [5–7]. Among the full-field simulation alternatives, the phase-field method is particularly well-suited to model coupled microstructure evolution [8–13]. It has been successfully applied to describe many thermo-chemo-mechanical processes including solidification [14], precipitation [15–17], fracture [18–21] and dislocation motion [22–24]. Further methodological developments including chemo-mechanical interface modelling and homogenisation have been treated recently in [25]. However, the majority of chemo-mechanical phase-field investigations are limited to linear elastic mechanics [10]. Until very recently, only few works have been carried out to fully couple the chemo-elasto-plastic processes in a thermodynamically consistent framework [20,21,26,27].

The use of diffuse-interface models to describe interfacial phenomena dates back to Cahn and Hilliard [28]. The original Cahn–Hilliard (CH) equation was used to model spinodal decomposition in binary alloys, but has since been extended to multi-component systems and coupled with microelasticity [11,29–32]. A critical challenge in simulating the thermodynamics of multi-component chemo-mechanical systems is the numerical approximation of a generally non-convex chemical free energy. Numerical methods have been developed to solve such systems using finite difference [33], mixed finite element with composition and chemical potential treated as independent fields [34,35], isogeometric [36] and spectral [37] spatial discretisations. In the context of numerical time-integration, the stability, robustness and efficiency of the resulting solution algorithm is sensitive to the non-convexity of the chemical free energy. A successful approach in this regard is the splitting of the chemical free energy into concave and convex components, which are then approximated separately [38,39]. In particular, splitting methods have recently been applied to the multi-component, multi-phase CH equation with a generalised non-convex Landau energy [40,41]. In the context of a mixed finite-element-based weak formulation of the classic CH relation, Gomez and Hughes [35] employed a chemical energy splitting approach based on the sign of the fourth-order derivatives of the underlying energy functional. A recent mixed weak formulation of chemo-mechanics for two-phase, two-component finite-deformation gradient elastic solids based on unconditionally stable, second-order accurate time-integration and Taylor expansion of the non-convex energy has been given by Sagiyama et al. [42].

More recently, starting from a grand potential functional [43,44], the transport relations have been formulated for multi-component and multi-phase systems [45]. In such an approach, the thermodynamics of the system is set in a grand canonical ensemble and formulated in terms of the chemical potential. As a result, boundary and interface conditions based on the chemical potential [46], needed for a realistic representation of macroscopic systems where the total number of particles cannot be fixed, are naturally incorporated. However, these approaches are based on a Legendre transformation, which does not exist for more general non-convex forms of the chemical free energy. In this work, a convex splitting of the chemical free energy is instead used to invert the multi-component chemical potential–composition relation. This results in an expression for component transport in terms of the chemical potential rather than the chemical composition, analogous to the grand potential approach, but applicable to more general forms of the chemical free energy. This paper is organised as follows: the basic model formulation for a single phase elasto-viscoplastic solid is presented in Section 2, followed by an outline of its numerical implementation in Section 3. In particular, since a dissipation potential exists for the flux-force relations of the current model, the corresponding initial boundary-value problems (IBVP) can be formulated with the help of rate variational methods [47–49]. In Section 4 representative examples are used to benchmark and compare the proposed method with conventional transport relations. A summary is provided in Section 5 along with perspectives for future applications.

2. Model formulation

2.1. Basic relations

Let $\mathcal{B}_0 \subset \mathbb{R}^3$ be a microstructural domain of interest, with boundary $\partial \mathcal{B}_0$. Attention is restricted in this work to the case of a single-phase elasto-viscoplastic solid mixture of M diffusing chemical components. Component diffusion and reaction in the mixture are modelled as usual by the corresponding component mass or number balance relations

$$\dot{c}_m = -\operatorname{Div} \mathbf{j}_m + \sigma_m, \qquad \text{for} \quad m = 1, \dots, M, \tag{1}$$

in the mixture in terms of component (mass or number) concentration $0 \leq c_m \leq 1$, the corresponding flux density $\mathbf{j}_m$, and the corresponding specific supply-rate, σ_m. Assuming that the mixture is closed with respect to constituent

mass or number, the corresponding sum relations

$$1 = \sum_{m=1}^{M} c_m, \quad \mathbf{0} = \sum_{m=1}^{M} \mathbf{j}_m, \quad 0 = \sum_{m=1}^{M} \sigma_m, \tag{2}$$

and (1) imply $\sum_{m=1}^{M} \dot{c}_m = 0$.

Besides this, the deformation resulting from an applied loading defines a field $\chi(\mathbf{x}) : \mathbf{x} \in \mathcal{B}_0 \to \mathbf{y} \in \mathcal{B}$ mapping points $\mathbf{x}$ in the undeformed configuration $\mathcal{B}_0$ to points $\mathbf{y}$ in the deformed configuration $\mathcal{B}$. Following Shanthraj et al. [21], the total deformation gradient, given by $\mathbf{F} = \partial \chi / \partial \mathbf{x} = \nabla \chi$, is multiplicatively decomposed as

$$\mathbf{F} = \mathbf{F}_e \, \mathbf{F}_c \, \mathbf{F}_p, \tag{3}$$

where $\mathbf{F}_p$ is a lattice preserving isochoric mapping due to plastic deformation, $\mathbf{F}_c$ represents the local deformation due to solute misfit, and $\mathbf{F}_e$ is a mapping to the deformed configuration. In the current approach the stress relaxation due to the component diffusion process is captured through the stress-free deformation gradient, $\mathbf{F}_c$.

Restricting attention to isothermal and quasi-static processes with no external supplies of momentum or energy, the balance relations for linear momentum, angular momentum, and internal energy, are given by

$$\mathbf{0} = \operatorname{Div} \mathbf{P}, \quad \mathbf{P}^\mathrm{T} \mathbf{F} = \mathbf{P} \mathbf{F}^\mathrm{T}, \quad \dot{\varepsilon} = \mathbf{P} \cdot \dot{\mathbf{F}}, \tag{4}$$

where, $\mathbf{P}$ is the first Piola–Kirchhoff stress, and ε is the referential internal energy density. As well the balance relation,

$$\dot{\eta} = \theta^{-1} \delta - \theta^{-1} \operatorname{Div} \sum_{m=1}^{M} \mu_m \mathbf{j}_m + \theta^{-1} \sum_{m=1}^{M} \mu_m \sigma_m, \tag{5}$$

for the entropy holds (e.g., [50, Chapter 2]), with dissipation-rate density, δ, absolute temperature, θ, and the chemical potential, μ_m, of component m.

Combination of (1)–(5) yields the form

$$\delta = \mathbf{P} \cdot \dot{\mathbf{F}} + \sum_{m=1}^{M-1} \tilde{\mu}_m \dot{c}_m - \dot{\psi} - \sum_{m=1}^{M-1} \mathbf{j}_m \cdot \nabla \tilde{\mu}_m \tag{6}$$

for the dissipation-rate density in terms of $\tilde{\mu}_a := \mu_a - \mu_M$, and the free energy density of the mixture, $\psi := \varepsilon - \theta \eta$.

The current model formulation is based on the basic constitutive form

$$\psi \left(\mathbf{F}, \mathbf{F}_p, \mathbf{F}_c, c_m, \tilde{c}_m, \nabla \tilde{c}_m \right) = \psi_e \left(\mathbf{F}, \mathbf{F}_p, \mathbf{F}_c \right) + \psi_c \left(c_m, \tilde{c}_m, \nabla \tilde{c}_m \right), \tag{7}$$

for ψ in terms of elastic, ψ_e, and chemical, ψ_c, parts. A non-local field, $\tilde{c}_m$ for independent components, $m = 1, \ldots, M - 1$, is introduced to weakly enforce any dependence of the energy on chemical inhomogeneity through its gradient $\nabla \tilde{c}_m$ [51]. Modelling $\mathbf{P}$ and $\tilde{\mu}_m$ as purely energetic, i.e. work conjugate to $\mathbf{F}$ and c_m respectively, results in the constitutive relations

$$\tilde{\mu}_m = \partial_{c_m} \psi + \partial_{\mathbf{F}_c} \psi \cdot \partial_{c_m} \mathbf{F}_c, \quad \mathbf{P} = \partial_{\mathbf{F}} \psi. \tag{8}$$

Together, (6)–(8) result in the residual form

$$\delta = -\partial_{\mathbf{F}_p} \psi \cdot \dot{\mathbf{F}}_p - \sum_{m=1}^{M-1} \mathbf{j}_m \cdot \nabla \tilde{\mu}_m \tag{9}$$

for the dissipation-rate density.

2.2. Energetic constitutive relations

The elastic energy, ψ_e, is modelled here relative to the intermediate configuration by the form

$$\psi_e(\mathbf{F}, \mathbf{F}_p, \mathbf{F}_c) = \frac{1}{2} \, \mathbf{E}_e \cdot \mathbb{C} \, \mathbf{E}_e, \tag{10}$$

in terms of the Green–Lagrange strain measure

$$\mathbf{E}_e = \frac{1}{2}\mathbf{F}_c^{\ T}\left(\mathbf{F}_e^{\ T}\mathbf{F}_e - \mathbf{I}\right)\mathbf{F}_c, \tag{11}$$

and anisotropic elastic stiffness $\mathbb{C}$. The work conjugate second Piola–Kirchhoff stress is given by,

$$\mathbf{S} = \mathbb{C}\mathbf{E}_e. \tag{12}$$

The 1st Piola–Kirchhoff stress tensor, $\mathbf{P}$, is then related to $\mathbf{S}$ through

$$\mathbf{P} = \mathbf{F}_e\,\mathbf{F}_c\,\mathbf{S}\,\mathbf{F}_p^{\ -T}. \tag{13}$$

Further details are provided in [4].

2.2.1. Crystal plasticity

The plastic deformation gradient is given in terms of the plastic velocity gradient, $\mathbf{L}_p$, by the flow rule

$$\dot{\mathbf{F}}_p = \mathbf{L}_p\mathbf{F}_p, \tag{14}$$

where $\mathbf{L}_p$ is work conjugate with the Mandel stress in the plastic configuration,

$$\mathbf{M}_p = -\partial_{\mathbf{F}_p}\psi\mathbf{F}_p^{\ T} = (\mathbf{F}_e\mathbf{F}_c)^T\mathbf{F}_e\mathbf{F}_c\mathbf{S} \approx \mathbf{F}_c^{\ T}\mathbf{F}_c\mathbf{S}, \tag{15}$$

assuming small elastic strains. A crystal plasticity model is used, where the plastic velocity gradient $\mathbf{L}_p$ is composed of the slip rates $\dot{\gamma}^\alpha$ on crystallographic slip systems, which are indexed by α

$$\mathbf{L}_p = \dot{\mathbf{F}}_p\mathbf{F}_p^{\ -1} = \sum_\alpha \dot{\gamma}^\alpha\,\mathbf{s}^\alpha \otimes \mathbf{n}^\alpha, \tag{16}$$

where $\mathbf{s}^\alpha$ and $\mathbf{n}^\alpha$ are unit vectors along the slip direction and slip plane normal, respectively [52,53]. The slip rates are given by the phenomenological description of Peirce et al. [54],

$$\dot{\gamma}^\alpha = \dot{\gamma}_0 \left|\frac{\tau^\alpha}{g^\alpha}\right|^n \, \text{sgn}\,(\tau^\alpha), \tag{17}$$

in terms of the reference shear rate $\dot{\gamma}_0$, and strain-rate sensitivity exponent n. The slip resistances on each slip system, g^α, evolve asymptotically towards g_∞ with shear γ^β ($\beta = 1, \ldots, 12$) according to the relationship

$$\dot{g}^\alpha = \dot{\gamma}^\beta h_0 \left|1 - g^\beta/g_\infty\right|^a \, \text{sgn}\left(1 - g^\beta/g_\infty\right) h_{\alpha\beta}, \tag{18}$$

with parameters h_0 and a. The interaction between different slip systems is captured by the hardening matrix $h_{\alpha\beta}$.

The plastic dissipation rate density $-\partial_{\mathbf{F}_p}\psi \cdot \dot{\mathbf{F}}_p$ appearing in (9) can then be reduced to the simpler slip system based form

$$-\partial_{\mathbf{F}_p}\psi \cdot \dot{\mathbf{F}}_p = \sum_\alpha \tau^\alpha\,\dot{\gamma}^\alpha, \quad \text{where} \quad \tau^\alpha = \mathbf{M}_p \cdot (\mathbf{s}^\alpha \otimes \mathbf{n}^\alpha). \tag{19}$$

On this basis, non-negativity of $\dot{\gamma}_0$, g_∞, h_0 and $h_{\alpha\beta}$ is sufficient to ensure non-negative plastic dissipation.

2.2.2. Multi-component chemo-mechanics

Following Hüter et al. [55], the local deformation arising from volumetric mismatch between solute components is given by

$$\mathbf{F}_c = \exp \sum_{m=1}^{M-1} v_m c_m \, \mathbf{I} \approx \mathbf{I} + \sum_{m=1}^{M-1} v_m c_m, \quad \text{for} \quad \sum_{m=1}^{M-1} v_m c_m \ll 1 \tag{20}$$

where the volumetric mismatch coefficient, v_m, is related to the Vegard's coefficient, *i.e.* $v_m = V_m/a_M$, where V_m is the Vegard's coefficient for component m dissolved as a solid solution in a matrix of component M, and a_M is the lattice parameter of the matrix.

The chemical energy, ψ_c, is modelled here using the following regular solution form

$$\Omega\psi_c(c_m, \tilde{c}_m, \nabla\tilde{c}_m) = \sum_{m=1}^{M-1} E_m^{sol} c_m + \sum_{m,n=1}^{M-1} E_{mn}^{int} c_m c_n + R\theta \sum_{m=1}^{M} c_m \ln c_m$$
$$+ \frac{1}{2}\sum_{m=1}^{M-1} \alpha_m (c_m - \tilde{c}_m)^2 + \frac{1}{2}\sum_{m=1}^{M-1} \kappa_m |\nabla\tilde{c}_m|^2, \tag{21}$$

where Ω is the molar volume; E_m^{sol}, κ_m and α_m are respectively the solution energy, gradient coefficient, and penalty parameter to weakly enforce $c_m = \tilde{c}_m$, for component m; E_{mn}^{int} is the interaction energy between component m and n; and R is the universal gas constant. The non-local field $\tilde{c}_m$ satisfies $\tilde{c}_m - \lambda_m^2 \, \mathrm{Div}\,\nabla\tilde{c}_m = c_m$ [51, Equation (19)] with $\lambda_m^2 = \kappa_m/\alpha_m$. This relation is equivalent to the equilibrium relation

$$0 = \delta_{\tilde{c}_m} \Omega\psi_c = \Omega\left(\partial_{\tilde{c}_m}\psi_c - \mathrm{Div}\,\partial_{\nabla\tilde{c}_m}\psi_c\right)$$
$$= \alpha_m(\tilde{c}_m - c_m) - \mathrm{Div}\,\kappa_m \nabla\tilde{c}_m. \tag{22}$$

from (21). Following Onsager [56], a linear flux-force form is assumed for the component diffusion,

$$\mathbf{j}_m = -M_m \nabla\tilde{\mu}_m, \tag{23}$$

with M_m the component mobility in the lattice-fixed frame of reference, and chemical potential, $\tilde{\mu}_m$, given by

$$\Omega\tilde{\mu}_m = E_m^{sol} + \sum_{n=1}^{M-1} E_{mn}^{int} c_n + R\theta \ln \frac{c_m}{c_M} + \alpha_m(c_m - \tilde{c}_m) - \Omega\nu_m \left(\mathbf{F}_c{}^{\mathrm{T}}\mathbf{S}\right)\cdot\mathbf{I}. \tag{24}$$

On this basis, non-negativity of M_m is sufficient to ensure non-negative dissipation due to component diffusion.

3. Numerical methods

The constitutive model introduced in Section 2 has been implemented in the freeware material simulation kit, DAMASK [4], and a large-scale parallel finite element (FE) code using the PETSc numerical library [57] has been developed to handle the discretisation and numerical solution of the coupled field equations.

3.1. Rate variational formulation of the initial boundary-value problems

The following represents a special case of the variational treatment of combined Cahn–Hilliard and Allen–Cahn modelling of finite-deformation gradient elastic solids in [58].

As detailed in [47], a rate-variational-based formulation of the IBVPs is contingent in particular on the existence of a dissipation potential for the model in question. In the current case, the force-based form

$$d = \frac{1}{n+1}\sum_\alpha g^\alpha \dot{\gamma}_0 \left|\frac{\tau^\alpha}{g^\alpha}\right|^{n+1} + \frac{1}{2}\sum_{m=1}^{M-1} \nabla\tilde{\mu}_m \cdot M_m \nabla\tilde{\mu}_m, \tag{25}$$

of this potential, d, determines the fluxes $\dot{\gamma}^\alpha = \partial_{\tau_\alpha} d$ and $\mathbf{j}_m = -\partial_{\nabla\tilde{\mu}_m} d$, consistent with (17) and (23), respectively. The convexity of d in the forces, and its non-negativity $d \geqslant 0$, together imply $\delta \geqslant 0$ in the context of (9). Besides this potential, the rate-variational formulation is based on the energy storage-rate density, ζ, and the supply rate density, p_s. For the current model, this is given by

$$\zeta := \sum_{m=1}^{M-1}\left(\tilde{\mu}_m \dot{c}_m + \partial_{\tilde{c}_m}\psi\,\dot{\tilde{c}}_m\right) + \partial_{\nabla\chi}\psi \cdot \nabla\dot{\chi} - \sum_\alpha \tau_\alpha \dot{\gamma}_\alpha, \qquad p_s = \sum_{m=1}^{M-1} \tilde{\mu}_m \sigma_m. \tag{26}$$

Together, these determine the volumetric part of the rate functional

$$P = \int_{\mathcal{B}_0} p_v \, \mathrm{d}\mathbf{x} + \int_{\partial\mathcal{B}_0^f} p_f \, \mathrm{d}\mathbf{s}, \quad \text{where} \quad p_v = \zeta + d + p_s. \tag{27}$$

The flux boundary conditions on $\partial\mathcal{B}_0^{\mathbf{f}}$ is given by p_{f}. The first variation of P with respect to $\tilde{\mu}_m$, $\dot{\boldsymbol{\chi}}$, $\dot{\tilde{c}}_m$, and τ_α takes the form

$$
\begin{aligned}
\delta P = {} & \sum_{m=1}^{M-1} \int_{\mathcal{B}_0} \delta_{\tilde{\mu}_m} p_{\mathrm{v}} \delta\tilde{\mu}_m \ \mathrm{d}\mathbf{x} + \sum_{m=1}^{M-1} \int_{\partial\mathcal{B}_0^{\mathbf{f}}} \left(\partial_{\nabla\tilde{\mu}_m} p_{\mathrm{v}} \, \boldsymbol{n}_{\partial\mathcal{B}_0} + \partial_{\tilde{\mu}_m} p_{\mathrm{f}}\right) \delta\tilde{\mu}_m \ \mathrm{d}\mathbf{s} \\
& + \int_{\mathcal{B}_0} \delta_{\dot{\boldsymbol{\chi}}} p_{\mathrm{v}} \delta\dot{\boldsymbol{\chi}} \ \mathrm{d}\mathbf{x} + \int_{\partial\mathcal{B}_0^{\mathbf{f}}} \left(\partial_{\nabla\dot{\boldsymbol{\chi}}} p_{\mathrm{v}} \, \boldsymbol{n}_{\partial\mathcal{B}_0} + \partial_{\dot{\boldsymbol{\chi}}} p_{\mathrm{f}}\right) \delta\dot{\boldsymbol{\chi}} \ \mathrm{d}\mathbf{s} \\
& + \sum_{m=1}^{M-1} \int_{\mathcal{B}_0} \partial_{\dot{\tilde{c}}_m} p_{\mathrm{v}} \delta\dot{\tilde{c}}_m \ \mathrm{d}\mathbf{x} + \sum_{\alpha} \int_{\mathcal{B}_0} \partial_{\tau_\alpha} p_{\mathrm{v}} \delta\tau_\alpha \ \mathrm{d}\mathbf{x}
\end{aligned}
\tag{28}
$$

via integration by parts and the divergence theorem. Necessary for stationarity, $\delta P = 0$, of (28) are the weak forms for the field relations

$$
\begin{aligned}
& \int_{\mathcal{B}_0} \partial_{\nabla\boldsymbol{\chi}} \psi \cdot \nabla\delta\dot{\boldsymbol{\chi}} \ \mathrm{d}\mathbf{x} - \int_{\partial\mathcal{B}_0} \partial_{\dot{\boldsymbol{\chi}}} p_{\mathrm{f}} \delta\dot{\boldsymbol{\chi}} \ \mathrm{d}\mathbf{s} = 0, \\
& \int_{\mathcal{B}_0} \left[(\dot{c}_m - \sigma) \, \delta\tilde{\mu}_m + M_m \nabla\tilde{\mu}_m \cdot \nabla\delta\tilde{\mu}_m \right] \ \mathrm{d}\mathbf{x} = 0, \\
& \int_{\mathcal{B}_0} \left[\alpha_m \left(c_m - \tilde{c}_m \right) \delta\tilde{c}_m + \kappa_m \nabla\tilde{c}_m \cdot \nabla\delta\tilde{c}_m \right] \ \mathrm{d}\mathbf{x} = 0,
\end{aligned}
\tag{29}
$$

and constitutive relation $0 = -\dot{\gamma}^\alpha + \partial_{\tau_\alpha} d$.

3.2. Finite element implementation

The rate-variational formulation yields the weak form of the field relations required for their finite-element (FE) implementation. In particular, Eq. (29) yields directly the weak momentum balance relation

$$
\mathbf{0} = \int_{\mathcal{B}_0} \nabla\delta\dot{\boldsymbol{\chi}} \cdot \mathbf{P}\mathrm{d}\mathbf{x},
\tag{30}
$$

where $p_{\mathrm{f}} = 0$ is assumed for simplicity, the weak multi-component transport relation

$$
\int_{\mathcal{B}_0} \left[(\dot{c}_m - \sigma) \, \delta\tilde{\mu}_m + M_m \nabla\tilde{\mu}_m \cdot \nabla\delta\tilde{\mu}_m \right] \ \mathrm{d}\mathbf{x} = 0,
\tag{31}
$$

and the weak non-local relation

$$
\int_{\mathcal{B}_0} \left[\alpha_m \left(c_m - \tilde{c}_m \right) \delta\tilde{c}_m + \kappa_m \nabla\tilde{c}_m \cdot \nabla\delta\tilde{c}_m \right] \ \mathrm{d}\mathbf{x} = 0.
\tag{32}
$$

where $\delta\dot{\boldsymbol{\chi}}$, $\delta\tilde{\mu}_m$ and $\delta\dot{\tilde{c}}_m$ are the virtual deformation rate, chemical potential and non-local concentration fields respectively. No-flux boundary conditions are assumed for the sake of simplicity.

The deformation field, $\boldsymbol{\chi}\,(\mathbf{x})$, chemical potential, $\tilde{\mu}_m\,(\mathbf{x})$, and non-local concentration field, $\tilde{c}_m\,(\mathbf{x})$, in addition to their virtual counterparts are discretised using a FE basis of shape functions, N_i^{χ}, N_i^{μ}, $N_i^{\tilde{c}}$, $N_i^{\delta\dot{\chi}}$, $N_i^{\delta\mu}$, and $N_i^{\delta\tilde{c}}$, where $[\boldsymbol{\chi}]_i$, $[\tilde{\mu}_m]_i$, $[\tilde{c}_m]_i$, $[\delta\dot{\boldsymbol{\chi}}]_i$, $[\delta\tilde{\mu}_m]_i$, and $[\delta\tilde{c}_m]_i$ are the respective degrees of freedom. The corresponding discrete differential operator matrices are $\mathbf{B}_i^{\chi}$, $\mathbf{B}_i^{\mu}$, $\mathbf{B}_i^{\tilde{c}}$, $\mathbf{B}_i^{\delta\dot{\chi}}$, $\mathbf{B}_i^{\delta\mu}$ and $\mathbf{B}_i^{\delta\tilde{c}}$. Under these approximations, the weak form Eqs. (30) to (32) can be rewritten as

$$
\sum_i [\delta\dot{\boldsymbol{\chi}}]_i^T \underbrace{\int_{\mathcal{B}_0} [\mathbf{B}_i^{\delta\dot{\chi}}]^T \mathbf{P}\mathrm{d}\mathbf{x}}_{\mathcal{R}_i^{\mathrm{mech}}} = \mathbf{0},
\tag{33}
$$

$$
\sum_i [\delta\tilde{\mu}_m]_i^T \underbrace{\int_{\mathcal{B}_0} \left[[N_i^{\delta\mu}]^T \, (\dot{c}_m - \sigma_m) + [\mathbf{B}_i^{\delta\mu}]^T M_m \mathbf{B}_i^{\mu} [\tilde{\mu}_m]_i \right] \mathrm{d}\mathbf{x}}_{\mathcal{R}_{i,m}^{\mathrm{chem}}} = 0,
\tag{34}
$$

$$\sum_i [\delta \tilde{c}_m]_i^T \underbrace{\int_{\mathcal{B}_0} \left[[N_i^{\delta \tilde{c}}]^T \alpha_m \left(c_m - N_i^{\tilde{c}}[\tilde{c}_m]_i \right) + [\mathbf{B}_i^{\delta \tilde{c}}]^T \kappa_m \mathbf{B}_i^{\tilde{c}}[\tilde{c}_m]_i \right] d\mathbf{x}}_{\mathcal{R}_{i,m}^{\mathrm{NL}}} = 0, \tag{35}$$

which defines a non-linear system of equations for the unknowns $[\chi]_i$, $[\tilde{\mu}_m]_i$, and $[\tilde{c}_m]_i$. A time-discrete system of equations is obtained by using a backward Euler approximation

$$\dot{c}_m = \frac{c_m(t_n) - c_m(t_{n-1})}{\triangle t} \tag{36}$$

of the rate $\dot{c}_m$ in Eq. (34).

The solution approach followed in this work involves solving the coupled system of Eqs. (33) to (35) within a staggered iterative loop until a self consistent solution is achieved for a time increment.

3.3. Chemical potential solution

The solution of the coupled system of Eqs. (33) to (35), for the deformation field, χ, chemical potential, $\tilde{\mu}_m$, and non-local concentration field, $\tilde{c}_m$, requires the inversion of Eq. (24) in order to express $c_m := c_m(\tilde{\mu}_n)$ for $m, n = 1, \dots, M-1$. This is achieved algorithmically in the current work through a semi-implicit splitting of the chemical potential relation,

$$\tilde{\mu}_m(t_n) = \breve{\mu}_{\tilde{m}}(t_n) + \hat{\mu}_{\tilde{m}}(t_{n-1}), \tag{37}$$

into a convex

$$\Omega \breve{\mu}_{\tilde{m}}(t_n) = E_m^{sol} + R\theta \ln \frac{c_m(t_n)}{c_M(t_n)} + \alpha_m \left(c_m(t_n) - \tilde{c}_m \right) - \Omega \nu_m \left(\mathbf{F_c}^T \mathbf{S} \right) \cdot \mathbf{I}, \tag{38}$$

and non-convex, *i.e.*,

$$\Omega \hat{\mu}_{\tilde{m}}(t_{n-1}) = \sum_{n=1}^{M-1} E_{mn}^{int} c_n(t_{n-1}), \tag{39}$$

contribution. Eq. (38) can then be inverted to express $c_m(t_n)$ in terms of Eqs. (37) and (39), yielding,

$$c_m(t_n) = \frac{\exp\left(\frac{f_m - \alpha_m c_m(t_n)}{R\theta} \right)}{1 + \sum_{n=1}^{M-1} \exp\left(\frac{f_n - \alpha_n c_n(t_n)}{R\theta} \right)}, \tag{40}$$

where

$$f_m = \Omega \tilde{\mu}_m(t_n) - E_m^{sol} + \alpha_m \tilde{c}_m + \Omega \nu_m \left(\mathbf{F_c}^T \mathbf{S} \right) \cdot \mathbf{I}. \tag{41}$$

Eq. (40) is an implicit system of equations to be numerically solved for $c_m(t_n)$ for a given set $\tilde{\mu}_n(t_n)$. A fixed point iteration is employed, which is unconditionally convergent for $\alpha_m \geq 0$ as the fixed point operator, *i.e.* the RHS in Eq. (40), is guaranteed to be a contractive mapping.

4. Results and discussion

In this section, the developed chemo-mechanical model for multi-component finite-strain elasto-viscoplastic materials is validated, benchmarked and showcased through illustrative examples. Simulations of spinodal decomposition in the absence of mechanical deformation are firstly performed to study the accuracy, convergence and numerical performance of the new proposed numerical scheme for the CH model. Then, we use the fully coupled chemo-elasto-viscoplastic model to investigate the combined effects of diffusion, elastic stressed and plastic relaxation on the spinodal decomposition and coarsening.

4.1. Validation and benchmarking of the numerical scheme

Diffusion simulations in the absence of mechanical deformation are first performed to study the convergence, accuracy and performance of the proposed numerical scheme for the CH model.
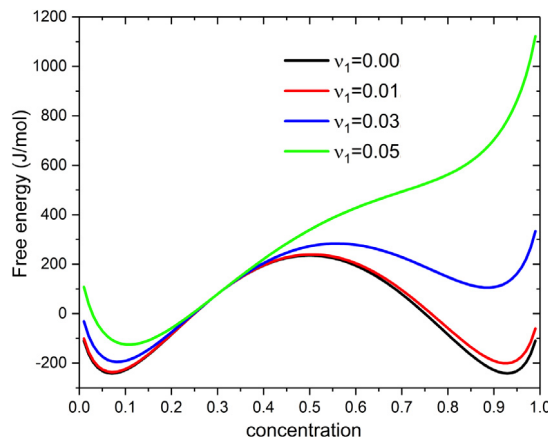
Fig. 1. Influence of the solute volumetric mismatch coefficient, ν_1, on the free energy, ψ, for $\nu_1 = 0.01, 0.03,$ and 0.05. It is assumed that the volumetric mismatch among solute components is accommodated by elastic deformation.

4.1.1. Convergence behaviour

A non-local concentration field, $\tilde{c}$, is introduced in the current model to account for the gradient energy contributions, thereby reducing the strong fourth-order CH PDE to two weakly coupled non-local second-order PDEs. The equivalence between the two methods is weakly enforced through the introduction of a penalty term. The convergence of the proposed method to the CH solution is discussed in this section. To investigate the effect of the penalty parameter, α, the gradient coefficient, κ, and the mesh size on the equilibrium numerical solution, we study one-dimensional (1-D) diffusion simulations without mechanical deformation. Since a semi-implicit time splitting method is proposed in this work to invert the non-convex chemical potentials relations, the influence of the time steps on the temporal accuracy of the numerical solutions is also studied in this section. Parameters for the chemical free energy density function in Eq. (21) are taken as $\Omega = 1 \times 10^{-5} \, \mathrm{m^3 \, mol^{-1}}$, $E_1^{sol} = 1.24 \times 10^4 \, \mathrm{J \, mol^{-1}}$, $E_{11}^{int} = -1.24 \times 10^4 \, \mathrm{J \, mol^{-1}}$, $\theta = 498 \, \mathrm{K}$, $\kappa_1 = 1 \times 10^{-16} \, \mathrm{J \, m^2 \, mol^{-1}}$, $M_1 = 2.2 \times 10^{-22} \, \mathrm{m^5 \, s^{-1} \, J^{-1}}$ and the penalty parameter α_1 is varied from 4×10^3 to $2.5 \times 10^6 \, \mathrm{J \, mol^{-1}}$. The resulting spinodal compositions are $c_\alpha = 0.07$ and $c_\beta = 0.93$, respectively. The chemical free energy without mechanical deformation of the studied system is represented by the black curve in Fig. 1. The minima in the double-well free energy curve represent the binodal compositions resulting from the decomposition of an initial homogeneous mixture. The inflection points of the free energy curve represent the spinodal below which spontaneous decomposition can occur.

The 1-D domain, $\mathcal{B}_0 = [0, 2L]$, is initialised into two regions, $\mathcal{B}_\alpha = [0, L)$ and $\mathcal{B}_\beta = (L, 2L]$. The initial concentrations for these two regions are taken as $c_\alpha = 0.49$ and $c_\beta = 0.51$, respectively, and the system size, $2L = 3 \, \mu\mathrm{m}$. To investigate the spatial convergence of the numerical solutions with mesh refinement, we discretise the domain with meshes varying from 60 to 2400 regular hexahedral elements and use a fixed time step of $\Delta t = 5 \, \mathrm{s}$. The temporal accuracy of the proposed formulation is studied by refining the time step from $\Delta t = 100 \, \mathrm{s}$ to $\Delta t = 2 \, \mathrm{s}$ using a fixed mesh of 300 elements.

The maximum of the pointwise difference between the concentration and non-local concentration fields, $\max_{x \in [0, 2L]} |c(x) - \tilde{c}(x)|$, is used here as a measure of convergence to the CH solution. Fig. 2(a) shows the convergence for different mesh sizes, at steady state, with increasing values of the penalty parameter. For both coarse and fine meshes, an exponential reduction in the difference, from 3.6×10^{-1} to 6.8×10^{-4}, is observed on increasing the penalty parameter from 4.0×10^3 to $2.5 \times 10^6 \, \mathrm{J \, mol^{-1}}$. For the lowest penalty parameter used, $\alpha = 4.0 \times 10^3 \, \mathrm{J \, mol^{-1}}$, the difference between concentration and non-local concentration is sensitive to the mesh size, and varies from 0.3 to 0.36 for mesh sizes varying from 150 to 2400 elements. However, when the penalty parameter is larger than $1.0 \times 10^4 \, \mathrm{J \, mol^{-1}}$, no distinguishable differences can be observed under different mesh sizes. Fig. 2(b) presents the variation of the interface width, d, with increasing the penalty parameter. The interface width converges to a constant value of 13 $\mu\mathrm{m}$ with minimal differences when the penalty parameter is larger than $1.0 \times 10^5 \, \mathrm{J \, mol^{-1}}$. It can be seen that for larger penalty parameters larger than $2.5 \times 10^4 \, \mathrm{J \, mol^{-1}}$, no distinguishable changes appear under mesh refinement from 300 to 2400 elements, giving good evidence of spatial convergence of

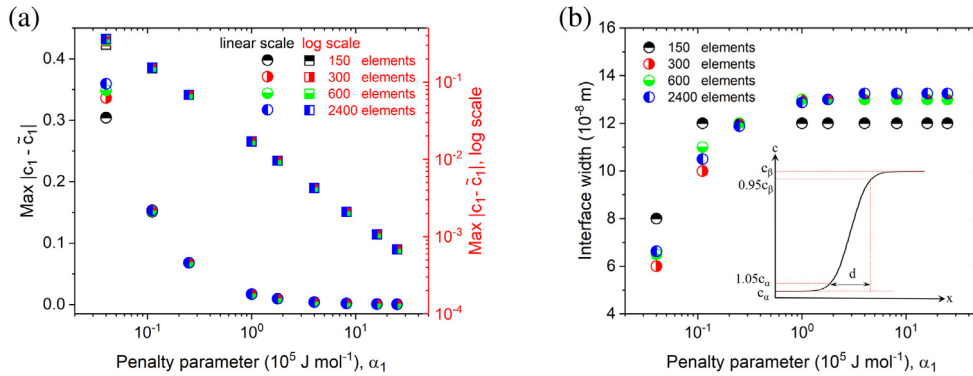**Fig. 2.** Influence of the penalty parameter, α_1, and mesh size on the numerical convergence and accuracy: (a) Convergence of the concentration, c, to the non-local concentration, $\tilde{c}$, as a function of the penalty parameter, α_1, ranging from 4×10^3 to 2.5×10^6 J mol^{-1}, in linear (round symbols) and log (square symbols) scale. (b) Relationship between the interface width and the penalty parameter at a constant gradient coefficient $\kappa_1 = 1 \times 10^{-16}$ J m^2 mol^{-1}. Schematic of the interface between binodal concentration c_α and c_β is given in the inset. The interface width d is defined as the distance where the concentration changes from $1.05c_\alpha$ to $0.95c_\beta$.

Fig. 3. Variation of the CPU time as a function of the penalty parameter, α_1.

the numerical solution. When the penalty parameter is smaller than 1.0×10^4 J mol^{-1}, no spatial convergence of the numerical solution is observed under mesh refinement. The convergence of the interface width in such studies is a good indicator for choosing an appropriate penalty parameter. Furthermore, to study the influence of the penalty parameter on the numerical efficiency, the variation of the CPU time spent on a single core of Intel Xeon Gold 6150 CPU 2.70 GHz with different penalty parameters is given in Fig. 3. It shows that the CPU time increases with increasing the value of the penalty parameter. The above simulations indicate that the penalty parameter should be chosen considering both the convergence of the numerical solution to the CH solution (Fig. 2(a)) and the numerical cost (Fig. 3). For practical purposes, a penalty parameter of 1×10^5 J mol^{-1} was found to give a good balance between convergence and numerical cost.

Fig. 4(a) shows the evolution of the maximum values of the concentration, indicating progress of the spinodal decomposition, for solutions obtained using a time step of $\Delta t = 100$ s, 20 s, 5 s and 2 s, respectively. While the large time step, $\Delta t = 100$ s, significantly delays the decomposition process implying insufficient temporal resolution, the absence of visible differences between the solutions for $\Delta t = 5$ s and 2 s indicates the convergence of the microstructure as time steps are refined. Fig. 4(b) shows the evolution of the maximum values of the concentration, for solutions corresponding to meshes with 60, 90, 150, 300 and 600 elements. Similar with the results in Fig. 2(b), no distinguishable differences can be observed beyond refinement from a mesh size of 300 elements, indicating the spatial convergence of the numerical solutions under mesh refinement.
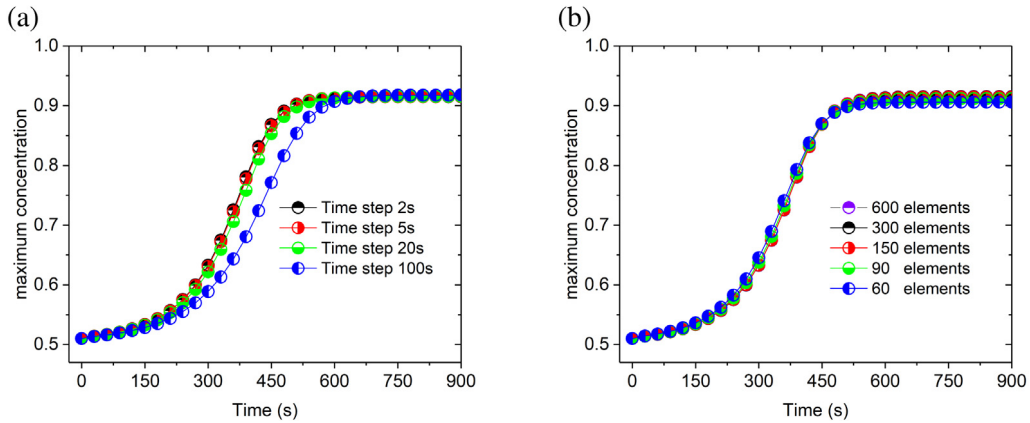
(a)

(b)

Fig. 4. Influence of the time steps and mesh size on the numerical convergence and accuracy: evolution of the maximum values of the concentration during the spinodal decomposition process where (a) time steps varying from 100 s to 2 s and (b) the mesh size varying from 60 to 600 elements.
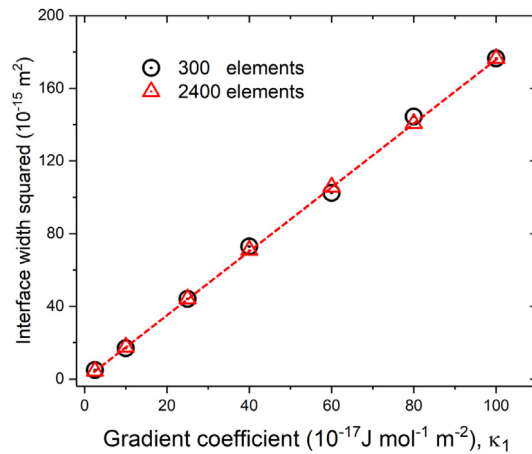
Fig. 5. Interface width squared, l^2, as a function of the gradient coefficient, κ_1 varying from 1×10^{-17} to 1×10^{-15} J m^2 mol^{-1}, obtained from simulations (round symbols with 300 elements and triangle symbols with 2400 elements) and compared with the ideal Cahn–Hilliard scaling (line).

The convergence of the proposed method is also characterised by investigating the relationship between the gradient coefficient, κ_m, and the interface width, d. Based on the classical CH theory [28], the gradient coefficient should have quadratic relationship with the interface width. Fig. 5 shows the simulated interface width squared as a function of the gradient coefficient at steady state. The gradient coefficient κ_1 varies from 1×10^{-17} to 1×10^{-15} J m^2 mol^{-1}. Note that for each simulation, the penalty parameter is chosen large enough to guarantee that the interface width converges to the constant value as discussed above. Fig. 5 verifies the linear relationship between the interface width squared and the gradient coefficient in both cases with coarse and fine meshes (300 and 2400 meshes, respectively), and shows that the penalty parameter does not affect the simulation results when it is sufficiently large. In the case with a mesh size with 300 elements, only a few points slightly deviate from the linear relationship. The above results indicate that the numerical solutions of the proposed approach converges to the CH solution, and the interface width is controlled solely by the physical parameters of the gradient coefficient, κ_m, for a sufficiently large penalty parameter, and guidelines for choosing the penalty parameter are provided.

4.1.2. Numerical performance

In this section, the accuracy and performance of the proposed numerical approach is compared to a conventional mixed FE CH solution scheme. A two-dimensional spinodal decomposition example in the absence of mechanical
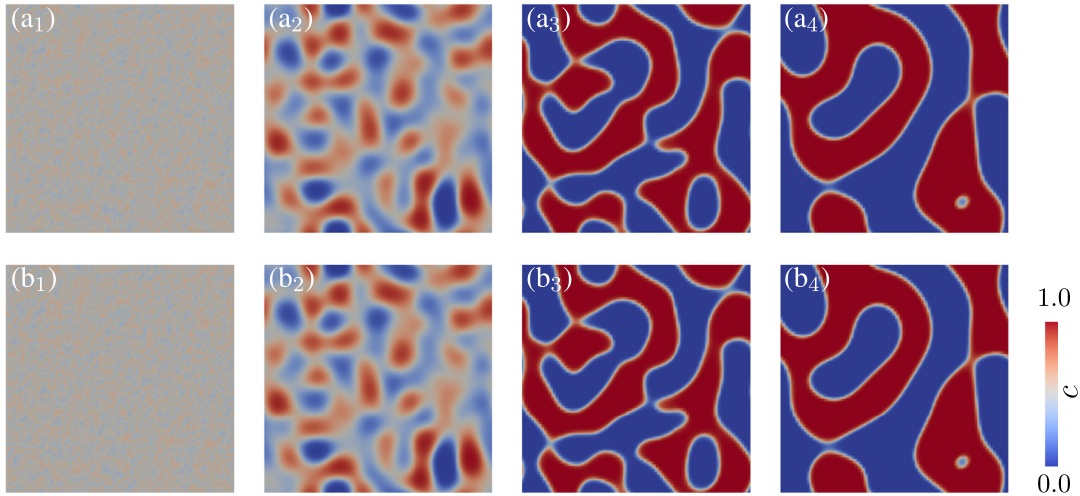
Fig. 6. Spinodal decomposition of a homogeneous solid solution with initial concentration of 0.5 and random perturbation of amplitude 0.1 at (1) 1 s, (2) 500 s, (3) 1000 s, and (4) 1800 s. The numerical implementations of the transport relations is based on (a) the concentration field and (b) the chemical potential field, respectively.
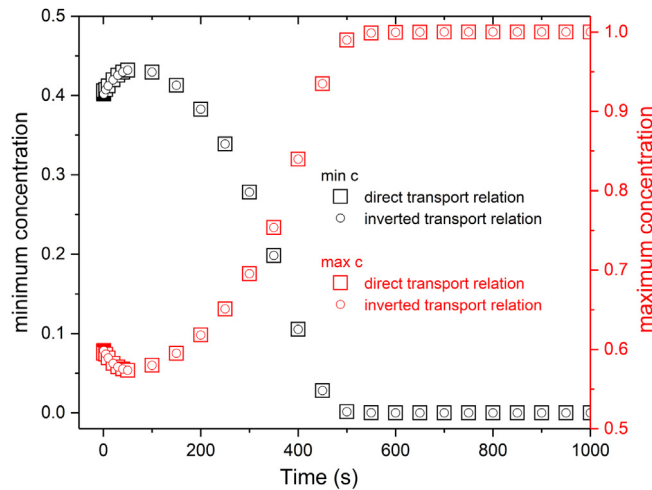

Fig. 7. Evolution of the maximum (red) and minimum (black) values of the concentration during the spinodal decomposition process obtained from classical (squares) and proposed (circles) numerical approaches, respectively.

deformation is solved to compare the two solution schemes. The model parameters used are as follows: $\Omega = 1 \times 10^{-5} \, \text{m}^3 \, \text{mol}^{-1}$, $E_1^{sol} = 2 \times 10^4 \, \text{J} \, \text{mol}^{-1}$, $E_{11}^{int} = -5 \times 10^4 \, \text{J} \, \text{mol}^{-1}$, $R\theta = 0.1 \times 10^4 \, \text{J} \, \text{mol}^{-1}$, $\kappa_1 = 1 \times 10^{-16} \, \text{J} \, \text{m}^2 \, \text{mol}^{-1}$, $M_m = 1.0 \times 10^{-22} \, \text{m}^5 \, \text{s}^{-1} \, \text{J}^{-1}$, $\alpha_1 = 5 \times 10^5 \, \text{J} \, \text{mol}^{-1}$. A square domain, $\mathcal{B}_0 = [0, L] \times [0, L]$, of size $L = 0.8 \, \mu\text{m}$ is meshed with 80×80 regular hexahedral elements. The initial concentration is taken as 0.5 with a random perturbation of amplitude 0.1.

Fig. 6 shows the temporal evolution of the concentration field during spinodal decomposition, starting from a homogeneous mixture with an average concentration of 0.5 and random perturbation with an amplitude of 0.1, into two spinodal compositions of 1.0×10^{-4} and 9.9×10^{-1}, determined by the minima of the free energy, ψ. Negligible differences in the concentration fields between the two solution approaches are observed. In order to quantitatively compare the simulation results, Fig. 7 shows the evolution of the maximum and minimum values of the concentration during the spinodal decomposition process, with spinodal decomposition initiating at 500 s. It can be seen that the simulated results for these two different approaches completely overlap during the entire spinodal
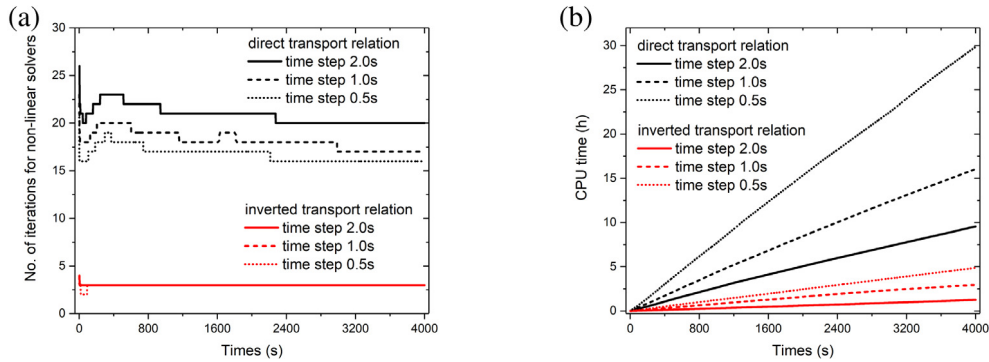
Fig. 8. Comparison of the (a) number of the Newton iterations per increment for convergence and (b) the overall CPU time during the simulation process to solve the direct (black lines) and the inverted (red lines) transport relations for three different time steps, 2.0 s, 1.0 s and 0.5 s.

decomposition process, thus validating the accuracy of the proposed numerical approach as a function of chemical potentials.

In order to compare the numerical performance of the two numerical approaches, the same Newton–Raphson scheme is used in the above simulations. The number of iterations required to obtain the solution for the nonlinear Newton–Raphson solver at each time step and the total CPU time spent on a single core of AMD Ryzen 3 PRO 1200 Quad-Core Processor 3.10 GHz during the spinodal decomposition process is used to quantify the performance and efficiency of the numerical scheme. The number of Newton iterations and the total CPU time for both approaches during the calculations is shown in Fig. 8. For all the time steps used in the numerical calculations (0.5 s, 1.0 s, 2.0 s), the number of Newton iterations required for the proposed solution method (2–4 iterations) is significantly lower than the number of Newton iterations required for the conventional mixed FE solution method (16–26 iterations). As shown in Fig. 8(b), the overall computation cost of the proposed method is much less and falls about 3 times below that of the corresponding conventional method. With decreasing the time step from 2.0 s to 0.5 s, the average number of the Newton iterations required for the conventional mixed FE solution method decreases from 21 to 16 iterations. Correspondingly, the number of the Newton iterations required for the proposed solution method only shows a decrease from 3 to 2 iterations at the beginning of the simulation process. In general, the proposed method requires 3 iterations on average and is almost independent on the time steps in the range of the time steps sizes used in the current simulations. Although the refinement of the time step does not lead to the obvious decrease of the number of the Newton iterations in the proposed scheme, the required Newton iterations and the numerical computation cost are still substantially lower comparing to the direct transport relations. These comparisons demonstrate the significantly improved performance and efficiency of the proposed inverted numerical scheme based on the chemical potentials.

4.2. Chemo-mechanical coupling

In this section, the chemical diffusion model is coupled to a finite-strain mechanical model to study the role of mechanical deformation on the spinodal decomposition process. Both elastic and plastic deformation accompanying diffusion are considered in the simulations. The material parameters for the chemical energy and crystal plasticity model are listed in Table 1. To illustrate the effect of mechanical deformation, through the deformation arising from volumetric mismatch between solute components, $\mathbf{F}_c$ in Eq. (20), on the free energy of the system, Fig. 1 shows the free energy of a 1-D system with various values of the solute volumetric mismatch coefficient. Note that in this plot, it is assumed that the local deformation arising from volumetric mismatch among solute components can only be accommodated by elastic deformation. It can be seen, that in terms of kinetics, the driving force for spinodal decomposition decreases with increasing levels of volumetric mismatch. From an energetic point of view, the miscibility gap is also modified, with the solute-poor binodal being more energetically favoured.

A square domain, $\mathcal{B}_0 = [0, L] \times [0, L]$, of size $L = 2.56$ μm is meshed with 256×256 regular hexahedral elements. Periodic boundary conditions on both concentrations and displacements were applied. The temporal

Table 1
Chemo-mechanical material parameters for the binary spinodal system. Ω is the molar volume, E_1^{sol} is the component solution energy, E_{11}^{int} is the component interaction energy, θ is the temperature, κ_1 is the gradient coefficient, α_1 is the penalty parameter, M_1 is the component mobility, $\dot{\gamma}_0$ is the reference shear rate, n is the strain-rate sensitivity exponent, g_0 and g_∞ are the initial and asymptotic slip resistances, and h_0 and $h_{\alpha\beta}$ are hardening parameters.

Chemical energy	Ω (m^3 mol^{-1})	E_1^{sol} (J mol^{-1})	E_{11}^{int} (J mol^{-1})	θ (K)	
	1×10^{-5}	1.24×10^4	-1.24×10^4	498	
	κ_1 (J m^2 mol^{-1})	α_1 (J mol^{-1})	M_1 (m^5 s^{-1} J^{-1})		
	2.5×10^{-17}	5×10^5	2.2×10^{-22}		
Crystal plasticity model	$\dot{\gamma}_0$ (s^{-1})	n	g_0 (MPa)	g_∞ (MPa)	a
	1×10^{-3}	20	31	63	2.25
	h_0 (MPa)	Coplanar $h_{\alpha\beta}$ (MPa)	Non-coplanar $h_{\alpha\beta}$ (MPa)		
	75	1	1.4		
Elastic constants	C_{11} (Pa)	C_{12} (Pa)	C_{44} (Pa)		
	1.06×10^{11}	6.0×10^{10}	2.8×10^{10}		

evolution of the concentration field during the spinodal decomposition process, in the absence of mechanical deformation (*i.e.* setting $\nu_1 = 0.00$), is shown in Fig. 9(a). At the early stage of the spinodal decomposition, the initial homogeneous mixture decomposes into two regions with different compositions, following their corresponding composition branch on the generalised multi-well Landau energy landscape Fig. 9(a$_1$). The decomposition stage is driven by the minimisation of the chemical free energy. Following decomposition, capillary-driven coarsening can be observed from Fig. 9(a$_2$) to (a$_4$), which is driven by the minimisation of interface energy, that occurs at a longer time scale compared to the initial decomposition stage.

The effect of the volumetric mismatch between solute components on spinodal decomposition and coarsening is investigated by first considering the case of an elastically deforming material. The volumetric mismatch coefficient, ν_1, is varied between 0.01 and 0.05, and the material parameters used are listed in Table 1. The temporal evolution of the concentration field during spinodal decomposition is shown in Fig. 9(b) to (d). It can be seen that the decomposition is minimally affected when the solute induced deformation is relatively small (*i.e.*, $\nu_1 = 0.01$), comparing Fig. 9(a) and (b). However, as the volumetric mismatch coefficient increases, the spinodal decomposition kinetics is significantly reduced, as shown in Fig. 9(c) and (d). This is due to the increasing elastic energy contribution to the driving force, which has the effect of suppressing the spinodal decomposition (Fig. 1). The binodal compositions are also affected by the chemo-mechanical coupling, with the solute-rich binodal point decreasing from 0.93 to 0.82 when the volumetric mismatch coefficient increases up to 0.05. Furthermore, one can observe that the morphology of the solute-rich region is also affected by the deformation arising from volumetric mismatch between solute components, comparing Fig. 9(a) and (d). In the absence of mechanical coupling, the solute-rich regions exhibit a spherical morphology due to the isotropic nature of the interface energy (Fig. 9(a$_4$)), but with increasing volumetric mismatch between solute components, the solute-rich regions are observed to order themselves along the softer directions of the cubically anisotropic elastic stiffness tensor used here (Fig. 9(d$_4$)).

To our knowledge, the numerical investigations of spinodal decomposition, presented in the literature, are limited to the coupling of elastic deformation with diffusion. The capability of the developed chemo-mechanical model allows us to also explore the more challenging influence of elasto-plasticity on the spinodal decomposition and coarsening, which is observed in materials applications such as rafting in superalloys [59] and hydride formation [60]. Parameters used for the crystal plasticity model are listed in Table 1.

The temporal evolution of the concentration field during spinodal decomposition on an elastic–plastically deforming material is shown in Fig. 10. Comparing Figs. 9 and 10 reveals that visco-plastic relaxation significantly affects the decomposition process. Spinodal decomposition is observed at 6000 s in the plastic material (Fig. 10(c$_3$)) compared to 10 000 s in the elastic material (Fig. 9 d$_4$), for the largest volumetric mismatch coefficient considered. In addition, the binodal compositions are close to those obtained from the simulations in the absence of mechanical
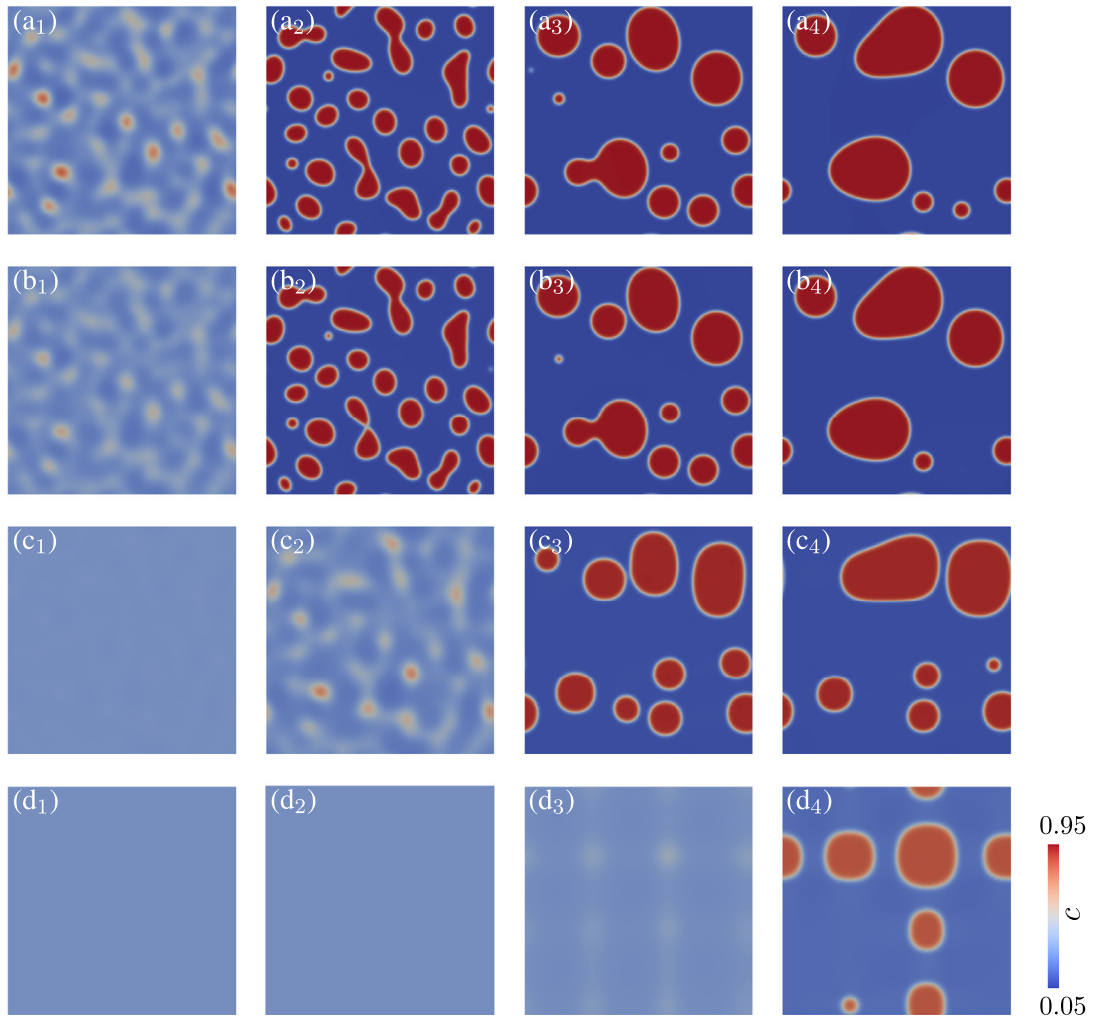
Fig. 9. Spinodal decomposition and coarsening (a) without volumetric mismatch between solute components, and with elastic accommodation of the volumetric mismatch between solute components, for mismatch strain coefficients of (b) $\nu_1 = 0.01$, (c) $\nu_1 = 0.03$, and (d) $\nu_1 = 0.05$, at time (1) 500 s, (2) 800 s, (3) 6000 s, and (4) 10 000 s.

deformation, since the deformation arising from volumetric mismatch between solute components can be effectively relaxed by the plastic deformation.

Fig. 11 presents the evolution of the hydrostatic stress and plastic strain for the cases with elastic-only and elasto-plastic deformation at a volumetric mismatch coefficient of 0.03. The plastic deformation relaxes the hydrostatic stress generated due to solute agglomeration during spinodal decomposition, and thus dissipates a significant portion of the stored elastic energy. The plastic strain localisation surrounding the solute-rich regions is observed, with a maximum value of 0.6. More interestingly, even though the spinodal compositions are similar to the case without mechanical deformation, the morphology of the solute-rich region differs significantly. When considering elasto-plastic deformation, the solute-rich regions exhibit an elliptic morphology at the intermediate level of volumetric misfit, as shown in Fig. 10(b_4). At the high levels of volumetric misfit, the solute-rich regions merge together and multiple lamellar regions can be observed, as shown in Fig. 10(c_4).

4.3. Ternary chemo-mechanical spinodal decomposition

In order to illustrate the applicability of the modelling approach to more complex material systems, a large three-dimensional (3D) simulation of a chemo-mechanically coupled ternary spinodal decomposition and coarsening
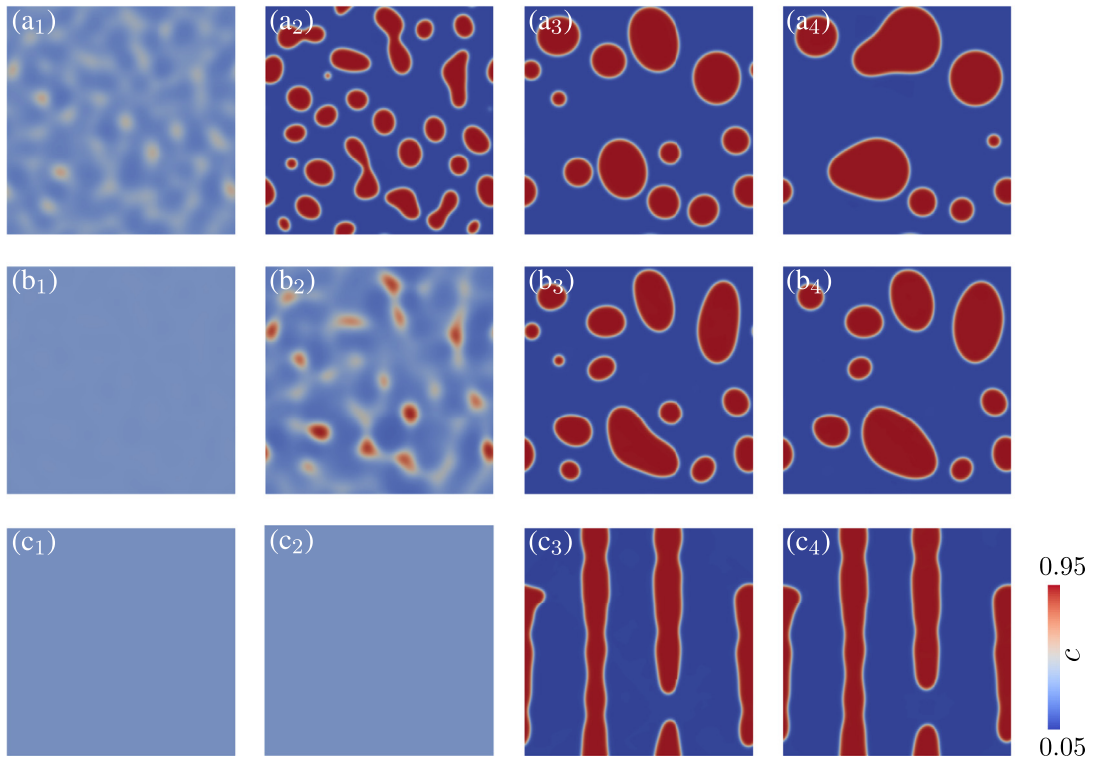
Fig. 10. Spinodal decomposition and coarsening with elasto-viscoplastic accommodation of the deformation due to the volumetric mismatch between solute components, for mismatch strain coefficients of, (a) $\nu_1 = 0.01$, (b) $\nu_1 = 0.03$, and (c) $\nu_1 = 0.05$, at time (1) 500 s, (2) 800 s, (3) 6000 s, and (4) 10 000 s.

Table 2
Chemical free energy parameters for the ternary spinodal system. Ω is the molar volume; E_A^{sol} and E_B^{sol} are the solution energies, κ_A and κ_B are the gradient coefficients, α_A and α_B are the penalty parameters, and M_A and M_B are the mobilities for component A and B respectively; E_{AA}^{int} and E_{AB}^{int} are the $A-A$ and $A-B$ interaction energies; and θ is the temperature.

Parameter	Value	Parameter	Value
Ω	1×10^{-5} (m^3 mol^{-1})	κ_A	1×10^{-18} (J m^2 mol^{-1})
E_A^{sol}	1.24×10^4 (J mol^{-1})	κ_B	1×10^{-18} (J m^2 mol^{-1})
E_B^{sol}	1.24×10^4 (J mol^{-1})	α_A	1×10^5 (J mol^{-1})
E_{AA}^{int}	-1.24×10^4 (J mol^{-1})	α_B	1×10^5 (J mol^{-1})
E_{AB}^{int}	-1.24×10^4 (J mol^{-1})	M_A	2.2×10^{-19} (m^5 s^{-1} J^{-1})
θ	498 (K)	M_B	2.2×10^{-19} (m^5 s^{-1} J^{-1})

process is considered next. The cubic domain, $\mathcal{B}_0 = [0, L] \times [0, L] \times [0, L]$, of size $L = 1.28$ µm is meshed with $128 \times 128 \times 128$ regular hexahedral elements. The initial concentrations for solute A and B are 0.3 and 0.3, respectively, with a random perturbation of amplitude 0.01. The chemical free energy parameters are listed in Table 2, and the crystal plasticity material parameters are listed in Table 1. The chemical free energy parameters used will result in the formation of three decomposition regimes: (A-rich, B-poor), (A-poor, B-rich), and (A-poor, B-poor).

Fig. 12 shows the temporal evolution of the morphologies of different decomposition regimes, the accompanying hydrostatic stress, and the plastic strain. In this fully coupled 3D ternary spinodal-elastic-viscoplastic mechanical decomposition simulation, the separated regions exhibit inter-connected morphologies instead of the isolated islands like those in the 2D binary cases, as the three components have relatively the same concentrations (0.3, 0.3, 0.4),
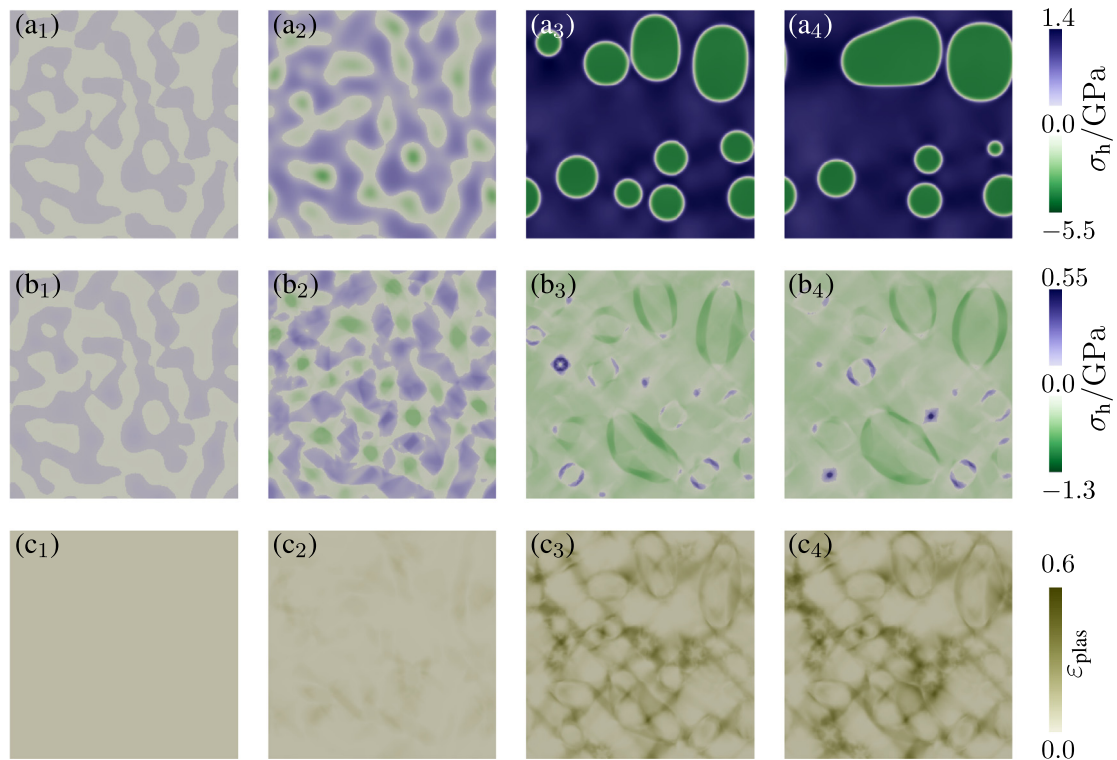
Fig. 11. Evolution of the hydrostatic stress during spinodal decomposition with (a) elastic, and (b) elasto-viscoplastic accommodation of the deformation due to the volumetric mismatch between solute components, and (c) the corresponding evolution of the plastic strain, for a mismatch strain coefficients of $\nu_1 = 0.03$, at time (1) 500 s, (2) 800 s, (3) 6000 s, and (4) 10 000 s.

close to the off-critical point. The hydrostatic stress distribution is significantly heterogeneous, even inside the same decomposition region, due to the accompanying plastic deformation, as shown in Fig. 12(b). It can be seen that the magnitude of the hydrostatic stress only changes slightly during the phase coarsening stage, while the total plastic strain increases gradually (Fig. 12(c)).

The corresponding 3D simulations of the ternary spinodal decomposition in the absence of mechanical deformation and only considering elastic deformation are presented in Fig. 13. Comparing Figs. 12(a) and 13, the separated regions produced by these three simulations exhibit qualitatively similar inter-connected morphologies. The approach of [61] could be used to quantify and distinguish the geometrical differences between these complicated patterns, however, a full discussion is beyond the scope of the current work and represents work in progress to be reported in the future.

5. Conclusions and outlook

In this work, a numerical approach has been introduced, using a semi-implicit convex splitting to invert the multi-component chemical potential relations, and resulting in a numerically advantageous expression for their transport in terms of the chemical potential. The approach is validated using a generalised spinodal Landau-type system as a benchmark, exposed to different chemo-mechanical starting and boundary conditions. A convergence of the proposed weakly non-local approach to the strong CH form is demonstrated with increasing values of the penalty parameter. However, for practical purposes, a penalty parameter of $1 \times 10^5 \, \mathrm{J\,mol^{-1}}$ was found to give sufficiently converged results. A significant reduction of the numerical cost and stability of the proposed approach is also demonstrated, allowing for the use of larger time steps in long-term diffusion simulations.

The influence of chemo-mechanical coupling, including both elastic and anisotropic crystalline plastic deformation, on the spinodal decomposition and coarsening process is also investigated. It is found that the stored elastic energy can narrow the miscibility gap and alter the binodal compositions. The decomposition kinetics is significantly
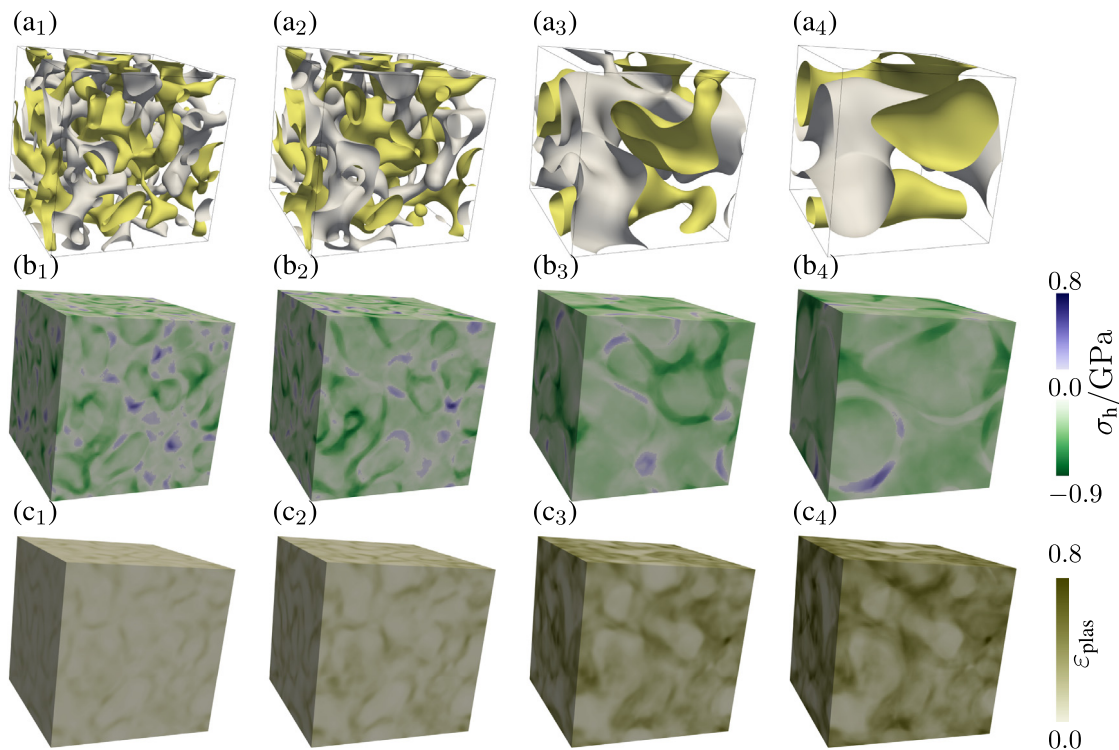
Fig. 12. Evolution of (a) the morphologies of the decomposition regions, (b) the hydrostatic stress, and (c) the plastic strain during a ternary spinodal decomposition and coarsening process, in a crystalline anisotropic elasto-plastic deforming material, with a mismatch strain coefficient of $\nu_1 = 0.03$, at time (1) 400 s, (2) 1000 s, (3) 6000 s, and (4) 15 000 s. The grey and yellow iso-surfaces represent (A-rich, B-poor) and (A-poor, B-rich) regions respectively, within the (A-poor, B-poor) matrix. The concentrations of the iso-surfaces for both solute A and B are taken as 0.9.
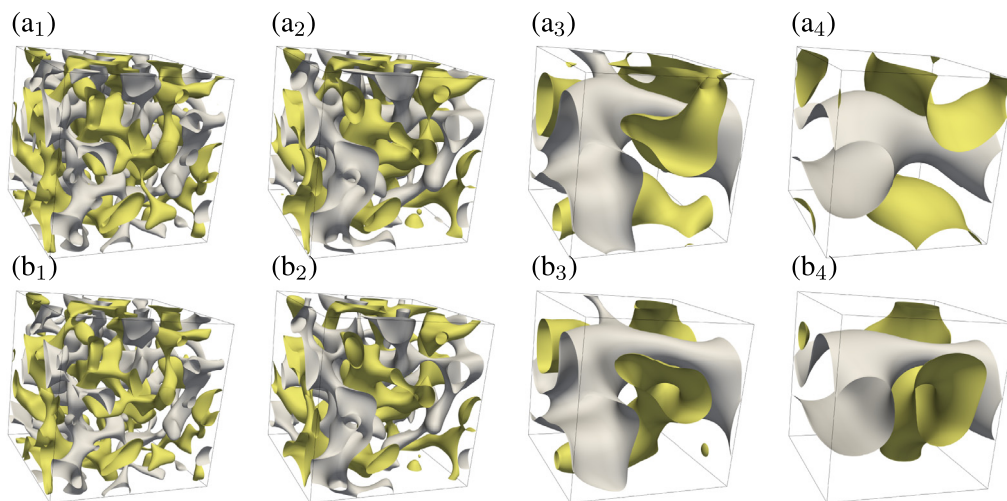

Fig. 13. Evolution of the spinodal decomposition and coarsening in a ternary spinodal decomposition and coarsening process, (a) without volumetric mismatch between solute components, and (b) considering elastic accommodation of the volumetric mismatch between solute components, with a volumetric mismatch coefficient of $\nu_1 = 0.03$, at time (1) 400 s, (2) 1000 s, (3) 6000 s, and (4) 15 000 s. The grey and yellow iso-surfaces represent (A-rich, B-poor) and (A-poor, B-rich) decomposition regions respectively, and the rest is (A-poor, B-poor) matrix. The concentrations of the iso-surfaces for both solute A and B are taken as 0.9.

reduced with increasing volumetric mismatch between solute components. Furthermore, the morphology of the solute-rich phase changes from spherical shape distributions to an ordered cubic distribution due to the anisotropy of the elastic stiffness tensor. When taking in to account additional visco-plastic relaxation of the volumetric mismatch, as in the case of realistic materials applications, it is found that the plastic relaxation accounts for a significant amount of the dissipated total energy. The spinodal compositions are close to those in the absence of mechanical deformation, but the solute-rich regions tend to coalesce into elongated lamellar morphologies.

Extension of the proposed approach to multi-phase systems is straightforward. This will be interesting as, in the context of multiphase systems, working directly with the chemical potential lends itself naturally to the Kim-Kim-Suzuki (KKS) description of interfaces [46], since, algorithmically, no partitioning of an average solute composition into the individual phases is required. The proposed approach is also particularly amenable to CALPHAD-based descriptions of the chemical energy [62], which is essential in the drive towards predictive simulations.

Declaration of competing interest

The authors declare that they have no known competing financial interests or personal relationships that could have appeared to influence the work reported in this paper.

Acknowledgements

References

[1] P. Shanthraj, M. Zikry, Optimal microstructures for martensitic steels, J. Mater. Res. 27 (12) (2012) 1598–1611.

[2] Q. Wu, P. Shanthraj, M. Zikry, Modeling the heterogeneous effects of retained austenite on the behavior of martensitic high strength steels, in: Fracture Phenomena in Nature and Technology, Springer, 2014, pp. 241–252.

[3] C. Liu, P. Shanthraj, M. Diehl, F. Roters, S. Dong, J. Dong, W. Ding, D. Raabe, An integrated crystal plasticity–phase field model for spatially resolved twin nucleation, propagation, and growth in hexagonal materials, Int. J. Plast. 106 (2018) 203–227.

[4] F. Roters, M. Diehl, P. Shanthraj, P. Eisenlohr, C. Reuber, S.L. Wong, T. Maiti, A. Ebrahimi, T. Hochrainer, H.-O. Fabritius, et al., DAMASK–The Düsseldorf Advanced Material Simulation Kit for modeling multi-physics crystal plasticity, thermal, and damage phenomena from the single crystal up to the component scale, Comput. Mater. Sci. 158 (2019) 420–478.

[5] M. Obrovac, L. Krause, Reversible cycling of crystalline silicon powder, J. Electrochem. Soc. 154 (2) (2007) A103–A108.

[6] C. San Marchi, B.P. Somerday, S.L. Robinson, Permeability, solubility and diffusivity of hydrogen isotopes in stainless steels at high gas pressures, Int. J. Hydrogen Energy 32 (1) (2007) 100–116.

[7] M. Cottura, B. Appolaire, A. Finel, Y. Le Bouar, Coupling the phase field method for diffusive transformations with dislocation density-based crystal plasticity: Application to Ni-based superalloys, J. Mech. Phys. Solids 94 (2016) 473–489.

[8] W.J. Boettinger, J.A. Warren, C. Beckermann, A. Karma, Phase-field simulation of solidification, Annu. Rev. Mater. Res. 32 (1) (2002) 163–194.

[9] V. Vaithyanathan, L.Q. Chen, Coarsening of ordered intermetallic precipitates with coherency stress, Acta Mater. 50 (16) (2002) 4061–4073.

[10] L.-Q. Chen, Phase-field models for microstructure evolution, Annu. Rev. Mater. Sci. 32 (1) (2002) 113–140.

[11] N. Moelans, B. Blanpain, P. Wollants, An introduction to phase-field modeling of microstructure evolution, CALPHAD 32 (2) (2008) 268–294.

[12] H. Emmerich, Advances of and by phase-field modelling in condensed-matter physics, Adv. Phys. 57 (1) (2008) 1–87.

[13] I. Steinbach, Phase-field models in materials science, Model. Simul. Mater. Sci. Eng. 17 (7) (2009) 073001.

[14] B. Nestler, A. Wheeler, A multi-phase-field model of eutectic and peritectic alloys: numerical simulation of growth structures, Physica D 138 (1) (2000) 114–133.

[15] N. Zhou, C. Shen, M. Mills, Y. Wang, Large-scale three-dimensional phase field simulation of γ'-rafting and creep deformation, Phil. Mag. 90 (1–4) (2010) 405–436.

[16] A.M. Jokisaari, S.S. Naghavi, C. Wolverton, P.W. Voorhees, O.G. Heinonen, Predicting the morphologies of γ' precipitates in cobalt-based superalloys, Acta Mater. 141 (2017) 273–284.

[17] S. Rudraraju, A. Van der Ven, K. Garikipati, Mechanochemical spinodal decomposition: a phenomenological theory of phase transformations in multi-component, crystalline solids, npj Comput. Mater. 2 (2016) 16012.

[18] R. Spatschek, E. Brener, A. Karma, Phase field modeling of crack propagation, Phil. Mag. 91 (1) (2011) 75–95.

[19] D. Schneider, E. Schoof, Y. Huang, M. Selzer, B. Nestler, Phase-field modeling of crack propagation in multiphase systems, Comput. Methods Appl. Mech. Engrg. 312 (2017) 186–195.

[20] P. Shanthraj, L. Sharma, B. Svendsen, F. Roters, D. Raabe, A phase field model for damage in elasto-viscoplastic materials, Comput. Methods Appl. Mech. Engrg. 312 (2016) 167–185.

[21] P. Shanthraj, B. Svendsen, L. Sharma, F. Roters, D. Raabe, Elasto-viscoplastic phase field modelling of anisotropic cleavage fracture, J. Mech. Phys. Solids 99 (2017) 19–34.

[22] Y.U. Wang, Y. Jin, A. Cuitino, A. Khachaturyan, Nanoscale phase field microelasticity theory of dislocations: model and 3D simulations, Acta Mater. 49 (10) (2001) 1847–1857.

[23] C. Shen, Y. Wang, Phase field model of dislocation networks, Acta Mater. 51 (9) (2003) 2595–2610.

[24] J.R. Mianroodi, P. Shanthraj, P. Kontis, J. Cormier, B. Gault, B. Svendsen, D. Raabe, Atomistic phase field chemomechanical modeling of dislocation-solute-precipitate interaction in Ni–Al–Co, Acta Mater. 175 (2019) 250–261.

[25] B. Svendsen, P. Shanthraj, D. Raabe, Finite-deformation phase-field chemomechanics for multiphase, multicomponent solids, J. Mech. Phys. Solids 112 (2018) 619–636.

[26] D. Schneider, F. Schwab, E. Schoof, A. Reiter, C. Herrmann, M. Selzer, T. Böhlke, B. Nestler, On the stress calculation within phase-field approaches: a model for finite deformations, Comput. Mech. 60 (2) (2017) 203–217.

[27] C. Wang, M.A. Ali, S. Gao, J.V. Goerler, I. Steinbach, Combined phase-field crystal plasticity simulation of p-and n-type rafting in co-based superalloys, Acta Mater. 175 (2019) 21–34.

[28] J.W. Cahn, J.E. Hilliard, Free energy of a non-uniform system. I. Interfacial energy, J. Chem. Phys. 28 (1958) 258–267.

[29] S. Hu, L. Chen, A phase-field model for evolving microstructures with strong elastic inhomogeneity, Acta Mater. 49 (11) (2001) 1879–1890.

[30] F. Fischer, N. Simha, J. Svoboda, Kinetics of diffusional phase transformation in multicomponent elastic-plastic materials, J. Eng. Mater. Technol. 125 (3) (2003) 266–276.

[31] H. Garcke, On a Cahn-Hilliard model for phase separation with elastic misfit, in: Annales de l'IHP Analyse Non Linéaire, Vol. 22, 2005, pp. 165–185.

[32] I. Steinbach, M. Apel, Multi phase field model for solid state transformation with elastic strain, Physica D 217 (2) (2006) 153–160.

[33] D. Furihata, A stable and conservative finite difference scheme for the Cahn-Hilliard equation, Numer. Math. 87 (4) (2001) 675–699.

[34] J.W. Barrett, J.F. Blowey, H. Garcke, Finite element approximation of the Cahn–Hilliard equation with degenerate mobility, SIAM J. Numer. Anal. 37 (1) (1999) 286–318.

[35] H. Gomez, T.J.R. Hughes, Provably unconditionally stable, second-order time-accurate, mixed variational methods for phase-field models, J. Comput. Phys. 230 (2011) 5310–5327.

[36] H. Gomez, V.M. Calo, Y. Bazilevs, T.J. Hughes, Isogeometric analysis of the Cahn–Hilliard phase-field model, Comput. Methods Appl. Mech. Engrg. 197 (49) (2008) 4333–4352.

[37] J. Zhu, L.-Q. Chen, J. Shen, V. Tikare, Coarsening kinetics from a variable-mobility Cahn-Hilliard equation: Application of a semi-implicit fourier spectral method, Phys. Rev. E 60 (1999) 3564–3572.

[38] C.M. Elliott, A.M. Stuart, The global dynamics of discrete semilinear parabolic equations, SIAM J. Numer. Anal. 30 (1993) 1622–1663.

[39] D.J. Eyre, Unconditionally gradient stable time marching the Cahn-Hilliard equation, in: Computational & Mathematical Models of Microstructural Evolution (Symposium BB), Vol. 529, MRS Proceedings, 1998, pp. 39–46.

[40] F. Boyer, S. Minjeaud, Numerical schemes for a three component Cahn-Hilliard model, ESIAM J. Math. Model. Numer. Anal. 45 (2011) 697–738.

[41] R. Tavakoli, Unconditionally energy stable time stepping scheme for Cahn-Morral equation: Application to multi-component spinodal decomposition and optimal space tiling, J. Comput. Phys. 304 (2016) 441–464.

[42] K. Sagiyama, S. Rudraraju, K. Garikipati, Unconditionally stable, second-order accurate schemes for solid state phase transformations driven by mechano-chemical spinodal decomposition, Comput. Methods Appl. Mech. Engrg. 311 (2016) 556–575.

[43] M. Plapp, Unified derivation of phase-field models for alloy solidification from a grand-potential functional, Phys. Rev. E 84 (2011) 031601.

[44] A. Choudhury, B. Nestler, Grand-potential formulation for multicomponent phase transformations combined with thin-interface asymptotics of the double-obstacle potential, Phys. Rev. E 85 (2012) 021602.

[45] L.K. Aagesen, Y. Gao, D. Schwen, K. Ahmed, Grand-potential-based phase-field model for multiple phases, grains, and chemical components, Phys. Rev. E 98 (2) (2018) 023309.

[46] S.G. Kim, W.T. Kim, T. Suzuki, Phase-field model for binary alloys, Phys. Rev. E 60 (1999) 7186–7197.

[47] B. Svendsen, On the thermodynamic- and variational-based formulation of models for inelastic continua with internal lengthscales, Comput. Methods Appl. Mech. Engrg. 48 (2004) 5429–5452.

[48] C. Miehe, A multi-field incremental variational framework for gradient-extended standard dissipative solids, J. Mech. Phys. Solids 59 (2011) 898–923.

[49] C. Miehe, Variational gradient plasticity at finite strains. Part I: Mixed potentials for the evolution and update problems of gradient-extended dissipative solids, Comput. Methods Appl. Mech. Engrg. 268 (2014) 677–703.

[50] S. de Groot, P. Mazur, Non-Equlibrium Thermodynamics, North Holland Publishers, Amsterdam, 1962.

[51] R.L.J.M. Ubachs, P.J.G. Schreurs, M.G.D. Geers, Microstructure evolution of tin-lead solder, IEEE Trans. Compon. Packag. Technol. 27 (4) (2004) 635–642.

[52] F. Roters, P. Eisenlohr, L. Hantcherli, D. Tjahjanto, T. Bieler, D. Raabe, Overview of constitutive laws, kinematics, homogenization and multiscale methods in crystal plasticity finite-element modeling: Theory, experiments, applications, Acta Mater. 58 (4) (2010) 1152–1211.

[53] P. Shanthraj, M. Zikry, Dislocation density evolution and interactions in crystalline materials, Acta Mater. 59 (20) (2011) 7695–7702.

[54] D. Peirce, R. Asaro, A. Needleman, Material rate dependence and localized deformation in crystalline solids, Acta Metall. 31 (12) (1983) 1951–1976.

[55] C. Hüter, P. Shanthraj, E. McEniry, R. Spatschek, T. Hickel, A. Tehranchi, X. Guo, F. Roters, Multiscale modelling of hydrogen transport and segregation in polycrystalline steels, Metals 8 (6) (2018) 430.

[56] L. Onsager, Reciprocal relations in irreversible processes. I, Phys. Rev. 37 (1931) 405–426.

[57] S. Balay, S. Abhyankar, M.F. Adams, J. Brown, P. Brune, K. Buschelman, L. Dalcin, V. Eijkhout, W.D. Gropp, D. Kaushik, M.G. Knepley, L.C. McInnes, K. Rupp, B.F. Smith, S. Zampini, H. Zhang, PETSc users manual, 2015.

[58] S. Gladkov, B. Svendsen, Thermodynamic and rate variational formulation of models for inhomogeneous gradient materials with microstructure and application to phase field modeling, Acta Mech. Sinica 31 (2) (2015) 162–172.

[59] P. Kontis, Z. Li, D.M. Collins, J. Cormier, D. Raabe, B. Gault, The effect of chromium and cobalt segregation at dislocations on nickel-based superalloys, Scr. Mater. 145 (2018) 76–80.

[60] D. Korbmacher, J. von Pezold, S. Brinckmann, J. Neugebauer, C. Hüter, R. Spatschek, Modeling of phase equilibria in Ni-H: Bridging the atomistic with the continuum scale, Metals 8 (4) (2018) 280.

[61] M. Gameiro, K. Mischaikow, T. Wanner, Evolution of pattern complexity in the Cahn–Hilliard theory of phase separation, Acta Mater. 53 (3) (2005) 693–704.

[62] H. Lukas, S.G. Fries, B. Sundman, Computational Thermodynamics: The Calphad Method, Cambridge University press, 2007.